energies

MDPI

Article

Multi-Mode Control of a Bidirectional Converter for Battery Energy Storage System †

Kuo-Yuan Lo [1,*], Kuo-Hsiang Liu [1], Li-Xin Chen [1], Ching-Yu Chen [2], Chang-Heng Shih [1] and Jyun-Ting Lin [1]

[1] Department of Electrical Engineering, National Kaohsiung University of Science and Technology, Kaohsiung 807, Taiwan
[2] Institute of Nuclear Energy Research, Atomic Energy Council, Taoyuan 325207, Taiwan
* Correspondence: kylo@nkust.edu.tw
† The present work is an extension of the paper "An interleaved DAB converter for battery energy storage system" presented to IFEEC 2021 Conference, Taipei, Taiwan, 16–19 November.

Abstract: In this paper, a bidirectional converter with multi-mode control strategies is proposed for a battery energy storage system (BESS). This proposed converter, which is composed of a half-bridge-type dual-active-bridge (HBDAB) converter and an H-bridge inverter, is able to operate the BESS with different power conditions and achieve the DC–AC function for lower input DC voltage applications. For the HBDAB converter, the variable-frequency control (VFC) and phase-shift control (PSC) are both adopted to achieve zero-voltage switching over a wider power range and the battery module balance control capability for BESS, respectively. In addition, the interleaved configuration is used to reduce the current ripple and increase the overall current rating. For the H-bridge inverter, the unipolar control mode (UCM) and totem-pole control mode (TPCM) are adopted to manage the real and reactive current control under different AC grid conditions. The UCM offers a reduction in current ripple for real and reactive power control. The TPCM is able to eliminate switching losses and achieve higher conversion efficiency for pure real power control. Considering applications for battery energy storage systems, the principle of operation and voltage gain analysis are described. Finally, computer simulations and hardware experimental results from a prototype system are presented to verify the performance of the proposed converter with the different control strategies.

Keywords: DAB converter; totem-pole converter; battery energy storage system

Citation: Lo, K.-Y.; Liu, K.-H.; Chen, L.-X.; Chen, C.-Y.; Shih, C.-H.; Lin, J.-T. Multi-Mode Control of a Bidirectional Converter for Battery Energy Storage System. *Energies* **2022**, *15*, 8114. https://doi.org/10.3390/en15218114

Academic Editor: Carlos Miguel Costa

Received: 14 September 2022
Accepted: 28 October 2022
Published: 31 October 2022

1. Introduction

Since renewable energy has been the fastest-growing energy source in recent years, fluctuations of the high-penetration renewable energy will cause a negative impact on the power grid system for stability and reliability. The demand for information storage, calculation, and transmission is also increasing. To strengthen grid resilience and minimize the consequences of extreme climatic conditions, a battery energy storage system (BESS) is one feasible solution to smooth the power output of renewable energies resource and provide ancillary services that support the transmission and stabilize the grid. For the BESS converters, power supplies above the kW level are often required, and bridge converter topologies, which have a simple construction with high conversion efficiency, are suitable solutions [1–4].

Typically, the grid-connected inverter system of the BESS may need a step-up power converter stage and an H-bridge-type inverter stage to achieve the DC–AC function for lower input DC voltage applications. In order to implement the bidirectional step-up power converter for BESS, power control capabilities, high conversion efficiency, and high power density are necessary to ensure the quality of energy storage and voltage conversion applications. For the bidirectional step-up converter, CLLC converters could be solutions with full-bridge and half-bridge topologies [5–8]. Figure 1a shows a typical

CLLC converter that consists of two H-bridge converters, a high-frequency transformer, two resonant capacitors, and two resonant inductors for the voltage control. In addition, CLLC converters can achieve the zero-voltage switching (ZVS) condition with a wider load condition. The output voltage of CLLC converters can be obtained by designing the switching frequency, the impedance of the resonant tank, the transformer turns ratio, and load conditions. However, the resonant frequency may vary due to the variation in the component value in the resonant circuit. In [6], the comparison is performed analytically using a ZVS-focused design methodology for the resonant converter and dual-active-bridge (DAB) converter. It shows that the resonant current results in higher conduction losses at heavy load conditions. The resonant converter is the preferred solution for high-step-down applications where partial load operation is prioritized. For improving the secondary rectify efficiency, synchronous rectification (SR) topologies are often used to reduce the conduction loss. The complexity of the SR controller may result in an increase in cost and circuit complexity.

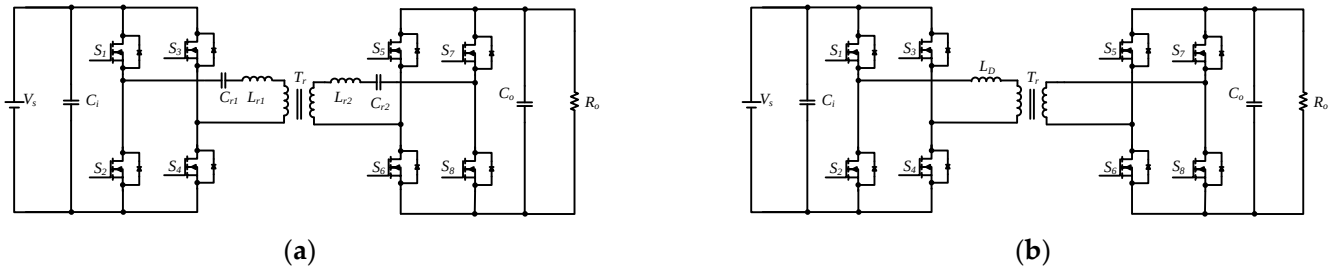

Figure 1. Bidirectional converters: (**a**) CLLC converter; (**b**) DAB converter.

Similar to the CLLC converter, the DAB converter is one of the solutions to achieve ZVS by controlling the switching frequency and different phase-shift angle between the bridges with galvanic isolation [9–17]. At heavy load conditions, DAB converters often have higher conversion efficiency for high power applications. In [15], the DAB scheme is used for solid-state transformers and maintains the advantages of conventional DAB, and obtains the bidirectional fault-handling capability for DC distribution applications. In [17], the design of modulating the phase-shift ratios is analyzed to suppress reactive power and increase the efficiency under non-unity voltage gain conditions. Global optimal phase-shift signals that minimize the reactive power under four different DAB operating scenarios are presented. A DAB converter often consists of two H-bridge converters, a high-frequency transformer, and a series inductor for the current control. Figure 1b shows a typical DAB converter. By adjusting the difference in the phase angles between the primary and secondary side H-bridge converter, the power flow control between the primary and secondary side is possible to be achieved [18–25]. In [21], a hybrid converter combining phase-shift full-bridge and half-bridge LLC resonant converters' configuration with shared zero-voltage switching lagging leg is proposed to ensure the switches in the lagging leg operating at fully ZVS condition. In [22], a novel control scheme of the bidirectional isolated DAB DC–DC converter is proposed to regulate the output voltage and current based on sliding mode (SM) control. However, the DAB converter has some disadvantages, such as the inability of the light load ZVS condition, circulating current loss, secondary side conduction loss, and ringing. Under the light load condition, the lead switch may miss the ZVS characteristic. In order to extend the load range for ZVS, decreasing the magnetizing inductance is one of the methods. However, more energy stored in the LC network results in an increase in the conduction losses for the switches. The intermittent operation is developed to improve conversion efficiency in light load conditions. By controlling the ratio of the power-transfer time to non-power-transfer time, the ZVS condition and conversion efficiency can be improved. Another method to extend the ZVS condition is using auxiliary circuits to achieve ZVS. Furthermore, the auxiliary circuits increase the circuit complexity with the cost impact. For the BESS applications, the methods presented

in the literature often need extra balancing circuits to connect each battery module, which results in a reduction in total efficiency and the increase in cost and circuit complexity. In this paper, the proposed bidirectional converter consists of multi-mode control strategies. Firstly, the variable-frequency control and phase-shift control are used to achieve the ZVS over a wider power range and the battery module balance control capability for BESS, respectively. The DAB converter can be designed as a full-bridge-type DAB (FBDAB) or half-bridge-type DAB (HBDAB) to implement the BESS power conversion. Considering the reduction in the switches, the HBDAB has benefits in terms of reduced corresponding driving circuits and cooling systems.

For the bidirectional DC–AC inverter, a full-bridge inverter with sinusoidal pulse width modulation (SPWM) is often used for grid-connected applications. Circuit simplicity is the main advantage of this type of inverter. However, the DC input voltage has to be higher than the peak value of the AC output voltage. Therefore, a step-up power converter is used to achieve the battery energy control for lower input DC voltage applications. To meet the relevant standards of high power factor and low total harmonic distortion (THD), a number of studies on bridge inverters are proposed [26–29]. However, there are several limitations of achieving the high cost and circuit simplicity. Further, the high-frequency switching of the switches may reduce the conversion efficiency of the system. Therefore, there are two operating modes developed in this paper: (1) unipolar control mode (UCM) and (2) totem-pole control mode (TPCM). The UCM is used to manage the real and reactive current control under different AC grid conditions. The proposed TPCM is able to eliminate the diode losses and achieve higher conversion efficiency for real power control.

Under three-phase balanced ac grid conditions, the DQ method is often used to simplify the design procedure and circuit analysis. However, due to the unsymmetrical transmission impedance, peak asymmetrical single-phase load, and random voltage faults, the unbalanced ac voltage situation often occurs in the real ac grid. Under unbalanced ac grid conditions, this negative sequence current generated from the grid-connected inverter may cause low-order torque pulsation and affect the stability of the power system. Four-wire inverter topologies are proposed in the literature to control the unbalanced current. Figure 2a shows a four-leg inverter topology to manage the neutral current. The Dq0 method is often used to control the DC components as a DC system model. However, the fourth leg may need to carry the huge unbalanced current under unbalanced ac grid conditions. Figure 2b shows three individual H-bridge inverters for controlling the unbalanced current. Because the outputs of the three phases are individual, all the maximum current stresses of the switches are the same in this system. In addition, the modulations for single-phase could be adopted to simplify the control design and circuit analysis. Although the higher number of devices is the major barrier for the inverter system, the low-rating switches can be implemented to improve the conversion efficiency.

This paper is an extended version of [30]. Compared with [30], the topology proposed in this paper uses another H-bridge inverter to achieve the bidirectional grid-connected converter system with multi-control strategies. It should be noted that an isolated transformer is often required to separate the inverters. In this paper, an isolated DAB converter is implemented to provide the step-up function and meet the regulations for the inverters. Therefore, the proposed converter is also suitable for a three-phase converter system under unbalanced ac grid conditions.

The proposed bidirectional converter system will be explained in Section 2. For the HBDAB converter, the variable-frequency control (VFC) and phase-shift control (PSC) will be described. Additionally, the principle of operation and voltage gain analysis of the HBDAB converter is systematically derived. For the H-bridge inverter, the multi-mode control is also designed to manage the real and reactive current control under different ac grid conditions. In Section 3, the performance of the proposed bidirectional converter is verified by using the experimental results. The digital signal processor (DSP) is used to fulfill the controller of the prototype converter. Section 4 concludes this paper.

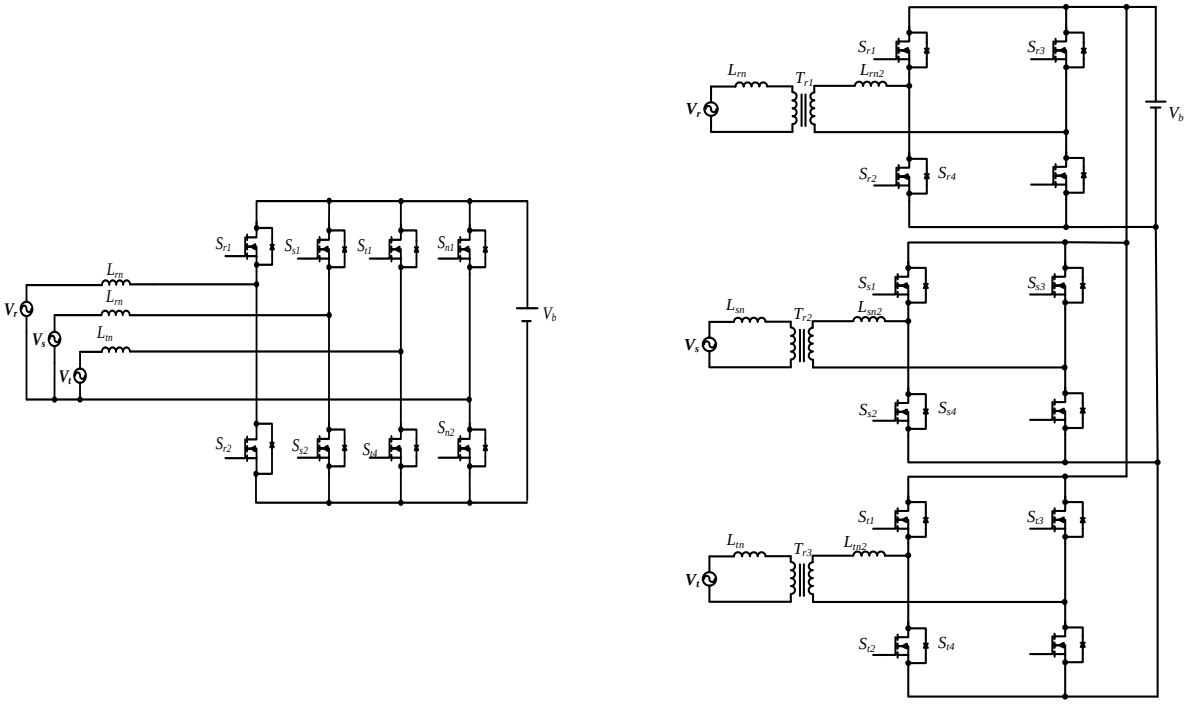

Figure 2. Three-phase inverter for an unbalanced ac grid system: (**a**) four-leg inverter topology; (**b**) three individual H-bridge inverters.

2. System Description

The circuit diagram for the proposed bidirectional converter is shown in Figure 3. It consists of two battery modules represented by the DC source, two HBDAB converters, and one H-bridge inverter with sinusoidal pulse width modulation. The H-bridge inverter is connected to the ac grid with an LCL filter, which avoids the resonance between the output capacitor and the parasitic inductor of grids. The H-bridge inverter switches (S_{r1}–S_{r4}) and HBDAB converter switches (S_1–S_8) are considered to use metal–oxide–semiconductor field-effect transistors (MOSFETs).

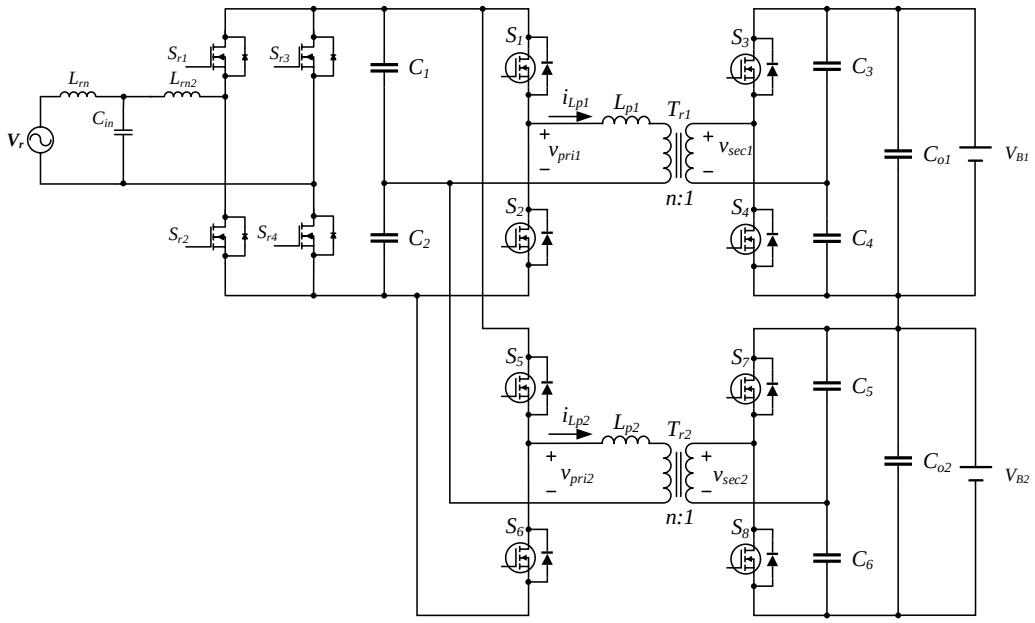

Figure 3. Circuit diagram for the proposed bidirectional DC–AC converter.

A. HBDAB converter and controller design

As shown in Figure 3, phase 1 HBDAB consists of four MOSFETs S_1–S_4, a transformer T_{r1}, a series inductor L_{p1}, and two-bridge capacitors C_1–C_4. The key waveforms of the proposed converter are shown in Figure 4. It is assumed that v_{pri1} and v_{sec1} are the output voltage of the primary and secondary phase 1 HBDAB; i_{Lp1} and i_{Lp2} are the currents through phase 1 and phase 2 series inductors. T_s is the output current ripple period, and it is equal to 1/2fs, where fs is the switching frequency. For the mode analysis, there are some assumptions to simplify the circuit analysis:

1. Transformers T_{r1} and T_{r2} are ideal, and n is the turns ratio defined by N_p/N_s.
2. In an HBDAB converter, all switches have the same duty cycle, and the voltages of the capacitors C_1 and C_2 are one-half of the input voltage.
3. All passive components are ideal for simplifying the mode analysis.
4. The analysis for the HBDAB converter is in a steady state.

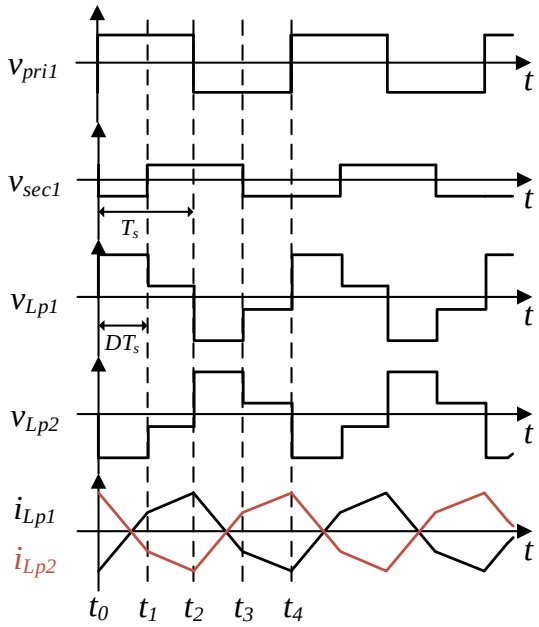

Figure 4. Key waveforms of the HBDAB converter.

A switching cycle can be divided into four modes. The equivalent circuit is shown in Figure 5.

Mode 1 [$t_0 < t < t_1$]: At the beginning of mode 1, S_1, S_4, S_6, and S_7 are turned on, and S_2, S_3, S_5, and S_8 are turned off. The inductor current i_{Lp1} flows through switches S_1 and S_4. The inductor current i_{Lp2} flows through switches S_6 and S_7. The voltage across v_{pri1} is equal to the voltage of capacitor C_1. In this mode, capacitors C_3 and C_6 are discharging, and C_4 and C_5 are charging by the stored energy in series inductors L_{p1} and L_{p2}. When i_{Lp1} decreases and changes its direction from a negative to a positive value, C_1 starts to discharge. When i_{Lp2} changes its direction from a positive to a negative value, C_2 starts to charge. Mode 1 ends when S_4 and S_7 are turned off.

Mode 2 [$t_1 < t < t_2$]: In this mode, the behavior of the primary side is the same as that in the previous mode. i_{Lp1} increases linearly while i_{Lp2} still decreases linearly. The inductor current is reflected by Tr_1 through the anti-parallel diodes of S_3 and S_8 because the S_4 and S_7 are turned off at t_1. During this period, S_3 and S_8 can be turned on with ZVS. This mode ends when S_1 and S_6 are turned off. In addition, i_{Lp1} reaches its positive peak value in this mode.

Mode 3 [$t_2 < t < t_3$]: In this mode, S_3 and S_8 are turned on, and S_1, S_2, S_4, S_5, S_6, and S_7 are turned off. The voltage across v_{pri1} is equal to the reverse voltage of capacitor C_2. The inductor current i_{Lp1} flows through the anti-parallel diodes of S_2, and the inductor

current i_{Lp2} flows through the anti-parallel diodes of S_5. During this period, S_2 and S_5 can be turned on with ZVS. In this mode, capacitors C_3 and C_6 are charged by stored energy in series inductors L_{p1} and L_{p2}. When i_{Lp1} changes its direction from a positive to a negative value, C_2 starts to discharge. When i_{Lp2} changes its direction from a negative to a positive value, C_1 starts to discharge. Mode 3 ends when S_3 and S_8 are turned off.

Mode 4 [$t_3 < t < t_4$]: In mode 4, the behavior of the primary side is the same as that in the previous mode. i_{Lp1} decreases linearly while i_{Lp2} still increases linearly. The secondary side current is through the anti-parallel diodes of S_4 and S_7 because the S_3 and S_8 are off at t_3. During this period, S_4 and S_7 can be turned on with ZVS. This mode ends when S_2 and S_5 are turned off. Furthermore, i_{Lp2} reaches its positive peak value in this mode. The following modes are similar to the previous operation modes as mentioned above.

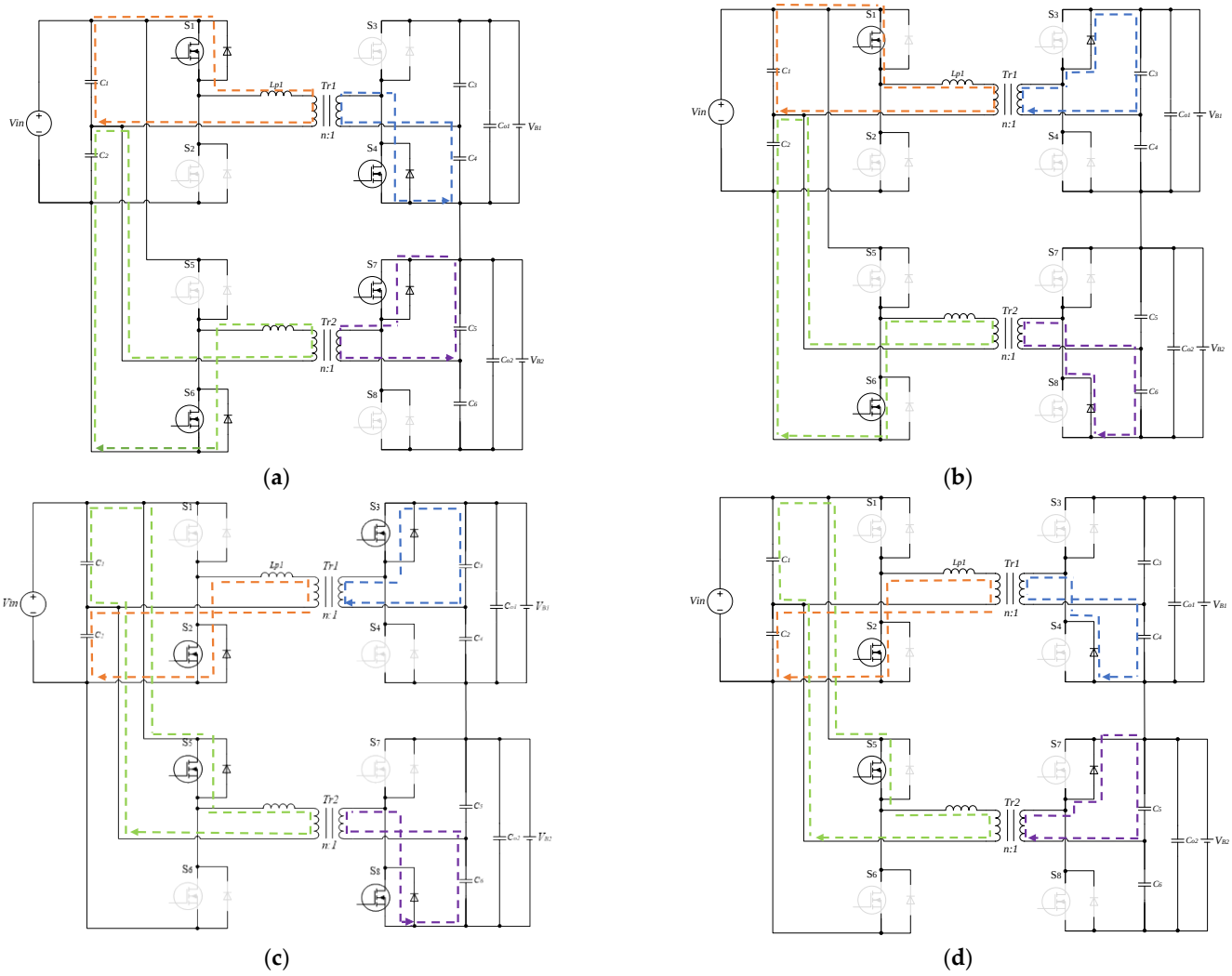

Figure 5. Operation modes of the HBDAB converter. (**a**) Mode 1 (**b**) Mode 2 (**c**) Mode 3 (**d**) Mode 4.

In the steady-state of the HBDAB converter, the inductor current i_{Lp1} at t_0, t_1, and t_2 can be derived as [31]:

$$i_{Lp1}(t_0) = \frac{-V_{in} + nV_{B1}(1-2\phi)}{4L_{p1}} T_s \quad (1)$$

$$i_{Lp1(t1)} = \frac{\frac{V_{in}}{2} + \frac{nV_{B1}}{2}}{L_{p1}} \phi T_s + i_{Lp1(t0)} \quad (2)$$

$$i_{Lp1(t2)} = \frac{\frac{V_{in}}{2} - \frac{nV_{B1}}{2}}{L_{p1}}(1-\phi)T_s + i_{Lp1(t1)} \tag{3}$$

where ϕ is the ratio of the phase-shift angle between the primary and secondary side, T_s is the switching period, *Vin* is the input voltage, V_{B1} is the battery voltage of module 1, n is the turns ratio of the transformer, and L_{p1} is the value of the inductor of module 1. The averaging inductor current can be obtained as:

$$I_{avg} = \left[\frac{nV_{B1}\phi(1-\phi)}{4L_{p1}f_{sw}}\right] \tag{4}$$

where f_{sw} is the switching frequency. Therefore, the output power and gain formula of each module can be obtained as:

$$P_{HBDAB1} = \frac{nV_{in}V_{B1}}{8L_{p1}f_{sw}}\phi(1-\phi) \tag{5}$$

$$\boldsymbol{G_{HBDAB} = \frac{nR_L}{8L_pf_{sw}}\phi(1-\phi)} \tag{6}$$

In Mode 1, i_{Lp1} is changed from negative to positive. To achieve the ZVS, the phase-shift angle ϕ condition can be obtained as:

$$\begin{cases} \phi \geq \frac{nG_{DAB}-1}{2G_{DAB}} & \text{for primary side ZVS} \\ \phi \geq \frac{1-nG_{DAB}}{2} & \text{for secondary side ZVS} \end{cases} \tag{7}$$

Based on these formulas, Figure 6 shows the ZVS region. Notice that the HBDAB is difficult to enter the ZVS region under a light-load situation with lowering the phase-shift duty. Therefore, under light load conditions, the converters may lose soft switching characteristics, which will cause large switching losses of the switches. Instead of using phase-shift modulation for the power flow control, a variable-frequency modulation is adopted in this paper. In order to ensure the ZVS condition in a wider load range, the phase-shift duty is set at a constant value of 0.5. The advantage of this control method is that the operating point always lies in the ZVS region, as shown in Figure 6. The variable-frequency modulation is used to control the overall output power. For the battery balance control, the phase-shift modulation is used to adjust the individual output power for each battery module. Therefore, low battery and DC-bus voltages can be accomplished.

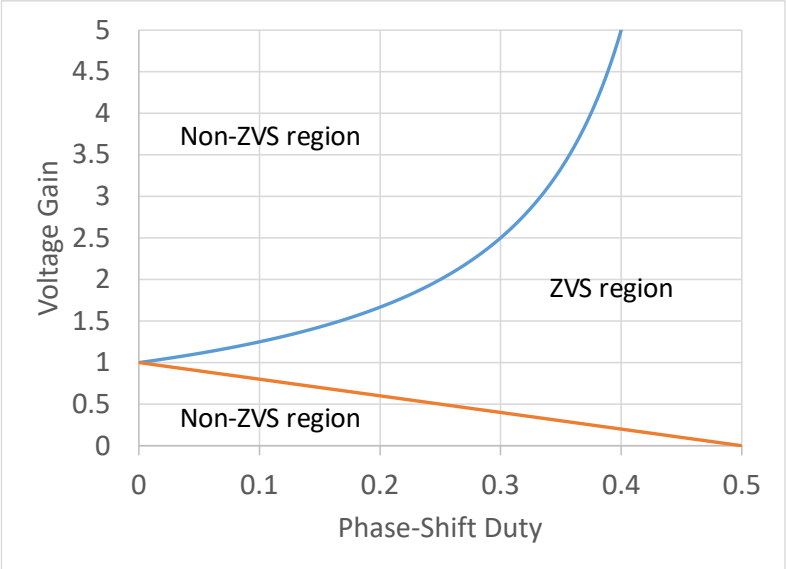

Figure 6. ZVS region of the HBDAB converters.

Figure 7 shows the control block diagram for the proposed HBDAB converter. V_{Tref} is the output voltage command. According to Equation (5), the total output power is controlled by the variable-frequency modulation with the feedback voltage loop of v_{TO}, which is the sum of the battery voltages v_{B1} and v_{B2}. For the voltage balance loop, individual phase-shift modulation is used to manage the unbalanced power between the battery modules with its own feedback voltage loop of v_{B1} and v_{B2}. In addition, the control signals have a 180-degree phase shifted to improve the input current waveforms contributed by each converter module.

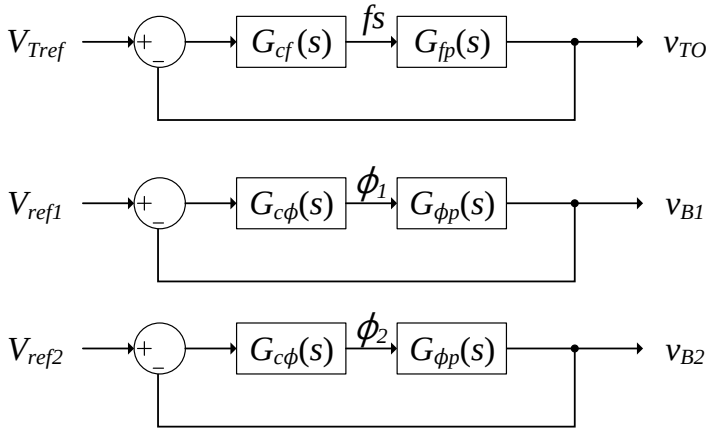

Figure 7. Control block diagram for the proposed HBDAB.

B. H-bridge inverter

The H-bridge inverter consists of four MOSFETs S_{r1}–S_{r4}. The HBDAB is connected to this grid-connected inverter, which has two operation modes: unipolar control mode (UCM) and totem-pole control mode (TPCM). In UCM, the grid-connected switch is turned on, and the inverter runs as a current source to provide real and reactive power. The control block diagram is shown in Figure 8 for the proposed H-bridge inverter system. The PR controller $G_{pr}(s)$ is designed to produce the equivalent duty cycle for the H-bridge inverter. The phase-locked loop (PLL) $H_V(s)$ is used for synchronizing with the grid frequency. The output current command input is generated by the PLL and the amplitude command of the output current I_m. The closed-loop transfer function of the grid voltage to the inverter output current can be expressed as:

$$T_{cv}(s) = \frac{i_{ac}(s)}{v_{ac}(s)} = \frac{\frac{H_v(s)}{V_m} I_m G_{pr}(s) F_m G_{ac}(s)}{1 + T_i(s)} + \frac{\frac{H_v(s)}{V_m} G_{cv}(s) F_m G_{ac}(s)}{1 + T_i(s)} - \frac{G_{iv}(s)}{1 + T_i(s)} \quad (8)$$

where $H_v(s)$, $G_{iv}(s)$, $G_{cv}(s)$, $G_{ac}(s)$, F_m, V_m, and $T_i(s)$ are the PLL gain, the current and voltage admittance terms, the plant transfer function, the controller gain, the amplitude of the grid voltage, and the open current loop transfer function, respectively. The open current loop transfer function can be expressed as:

$$T_i(s) = G_{pr}(s) F_m G_{ac}(s) H_i(s) \quad (9)$$

where $H_i(s)$ is the current feedback gain. The current controller $G_{pr}(s)$ is designed as a PR-type controller with the following gird frequency:

$$G_{pr}(s) = K_p + \frac{2K_r \omega_c s}{s^2 + 2\omega_c s + {\omega_o}^2} \quad (10)$$

where ω_c, ω_0, K_p, and K_r are the equivalent bandwidth, the resonance frequency, proportional gain, and resonant gain, respectively. Figure 9 shows the Bode plots of the current loop transfer function $T_i(s)$ with K_p = 0.05, K_r = 10, ω_c = 6.28 rad/s, and ω_0 = 377 rad/s. In UCM, the DC bus voltage of the inverter is 380 V, and the values of the output induc-

tor are 2.5 and 0.2 mH. This current controller can achieve a phase margin of 66 degrees with stability.

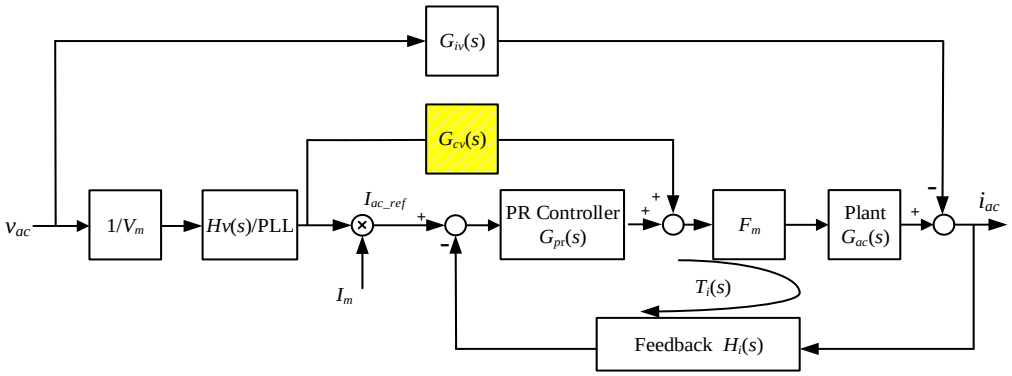

Figure 8. Control block diagram for the proposed H-bridge inverter.

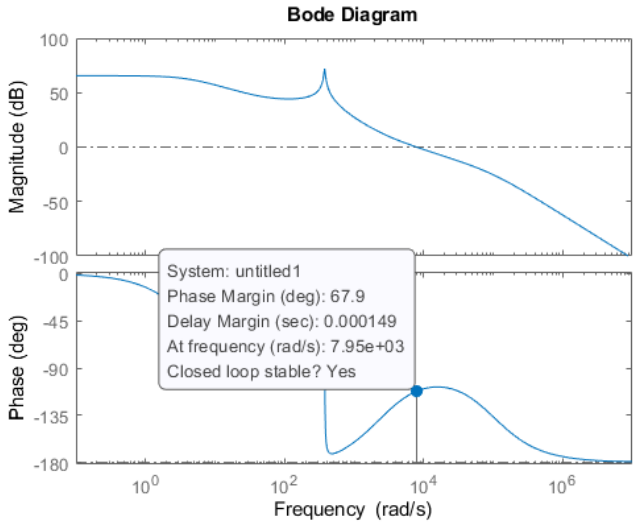

Figure 9. Bode plots of the open current loop transfer function.

In TPCM, the switches S_{r1} and S_{r2} are faster switching, and S_{r3} and S_{r4} are slower switching. The operation of the H-bridge inverter can be generally divided into different operation modes for improving conversion efficiency. The high-frequency switching leg is responsible for controlling the current of the output inductor. In other words, the switches can be designed as a pair of boost/buck converters in a half-line cycle of the grid voltage. During the positive half-cycle of the grid voltage, the switch S_{r4} is turned on while S_{r3} is turned off. For the negative half-cycle, switch S_{r3} is turned on, and switch S_{r4} is turned off. Since this low-frequency switching leg is only switched at zero crossing of the grid voltage, its switching loss can be neglected. Based on the following assumptions, the control waveforms of the H-bridge inverter in TPCM are shown in Figure 10. Figure 11 shows the typical waveforms of the high-frequency switching leg in TPCM. At $t = t_1$, the switch S_{r1} starts turning off. Meanwhile, the other switch S_{r2} remains off, and the inductor current starts discharging. Thus, the drain-to-source voltage of S_{r1} starts increasing to the output voltage until $t = t_2$. At $t = t_2$, S_{r2} starts turning on, and the inductor current discharges continuously until $t = t_3$. At $t = t_3$, S_{r2} starts turning off, and the drain-to-source voltage of S_{r1} starts decreasing until $t = t_4$. At $t = t_4$, S_{r1} is turned on. Meantime, the other switch S_{r2} remains off, and the inductor current starts charging.

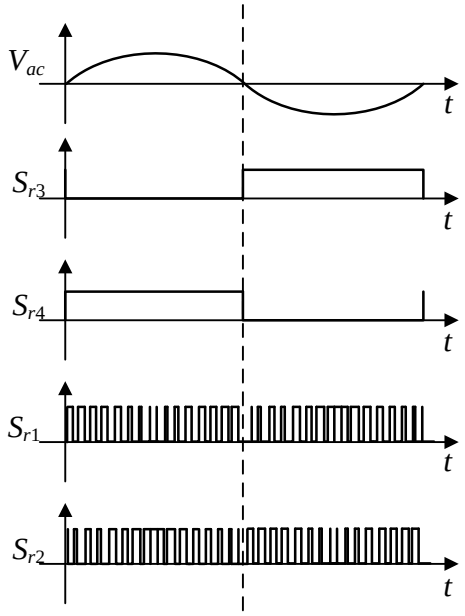

Figure 10. Control waveforms of the H-bridge inverter in TPCM.

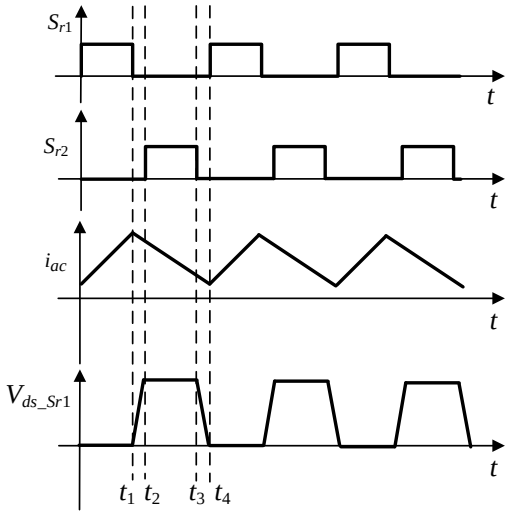

Figure 11. Typical waveforms of the high-frequency switching leg in TPCM.

The procedure of the mode transfers between grid-connected mode and standalone mode for the H-bridge inverter is shown in Figure 12. In the grid-connected mode operation, as soon as the reactive power command is near zero, the inverter enters TPCM. On the contrary, the inverter enters UCM if the reactive power is needed. Once the grid fault occurs, the H-bridge inverter is changed from the current source to the voltage source to compensate the voltage in the standalone mode. For an actual microenergy system, the converter's capacity should be large enough to supply the demand-load power in the standalone mode. Furthermore, the actual real/reactive power command should be set either by the interconnection requirements with the distribution system operator (DSO), or the applicable grid codes in the jurisdiction in which the microenergy system is operating [32].

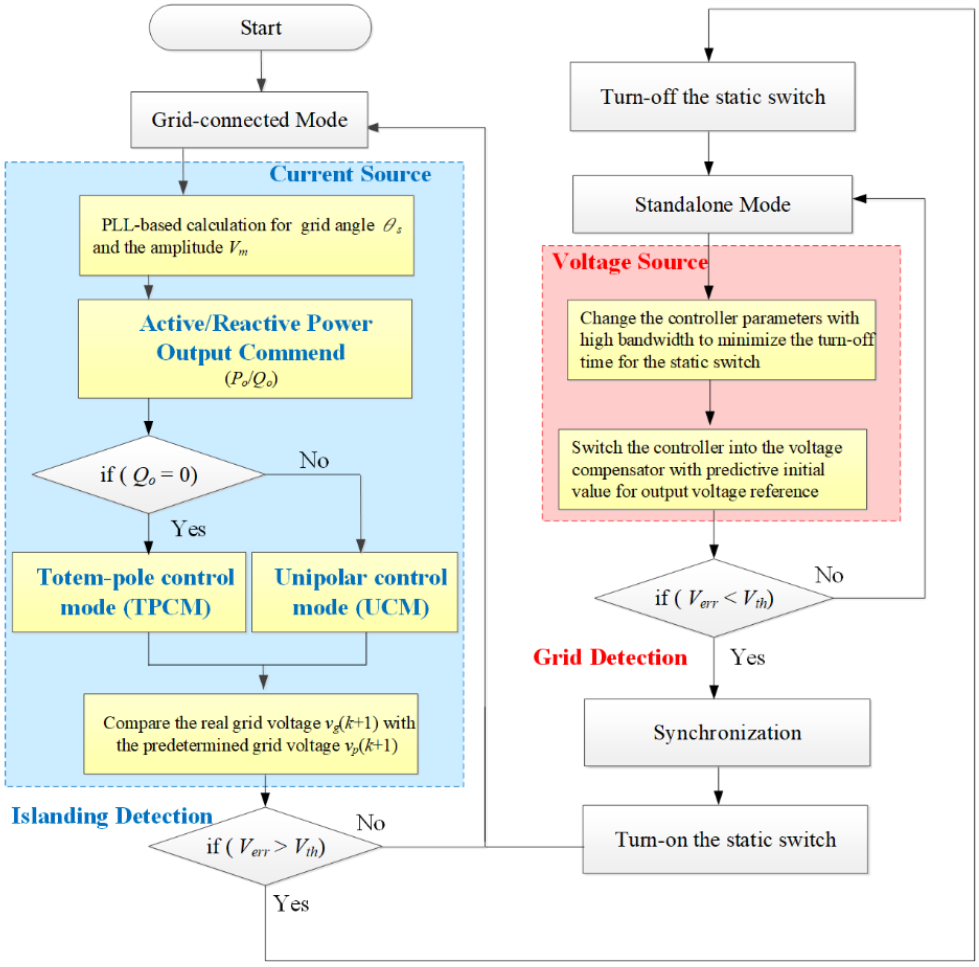

Figure 12. The procedure for the mode transfers between grid-connected mode and standalone mode for the H-bridge inverter.

3. Experimental Results

A prototype of the proposed bidirectional converter, which is composed of two sets of HBDAB modules and an H-bridge inverter, was built and tested with the multi-mode control strategies. The prototype specifications are listed in Table 1. Figure 13 shows the picture of the prototype converter with the proposed control strategies by using a DSP TMS320F28335. A voltage source in parallel with a resistor is used to estimate the battery charging and discharging for the HBDAB converter. Figure 14 shows the experimental waveforms of the gate-to-source and drain-to-source voltage waveforms for S_1 and S_2 to illustrate that ZVS can be achieved. The key experimental waveforms of the HBDAB converter are shown in Figures 15 and 16. Figure 15 illustrates the key waveforms of the series inductors. Figure 16 shows the experimental waveforms of the battery voltage and current of the transformers. It can be found that the experimental waveforms are consistent with the theoretical ones. In this paper, the proposed HBDAB converter is designed to control the output power individually for each battery module. To verify the individual control capability of the battery module, Figures 17 and 18 are presented the corresponding waveforms under the unbalanced power condition. In Figure 18, the battery voltage of module 1, v_{B1}, is about 206 V. The battery voltage of module 2, v_{B2}, is about 194 V. The individual phase-shift modulation is used to deal with the unbalanced current and voltage between the battery modules.

Table 1. Ratings and circuit parameters for the prototype converter.

Power rating	1 kW
Battery voltage, V_{B1} and V_{B1}	200 V_{dc}
Grid voltage, *Vac*	110 V_{ac}
Switching frequency for HBDAB, f_{sw}	30–60 kHz
Switching frequency for H-bridge inverter, f_s	20 kHz
Bridge capacitor (C_1, C_2, C_3, C_4, C_5, and C_6)	10 uF

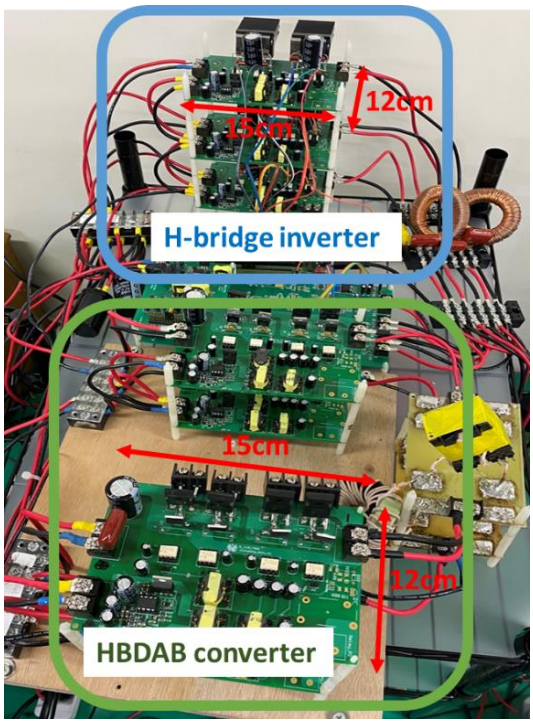

Figure 13. Prototype bidirectional converter for BESS.

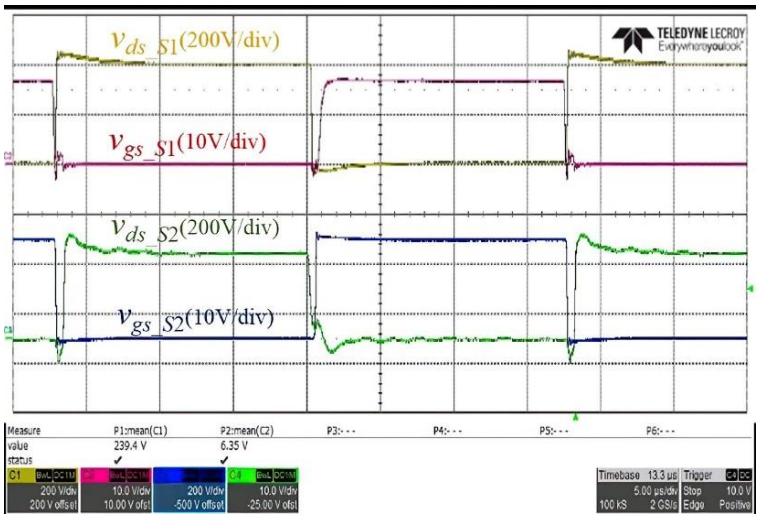

Figure 14. Experimental waveforms of the gate-to-source and drain-to-source voltage waveforms for S_1 and S_2.

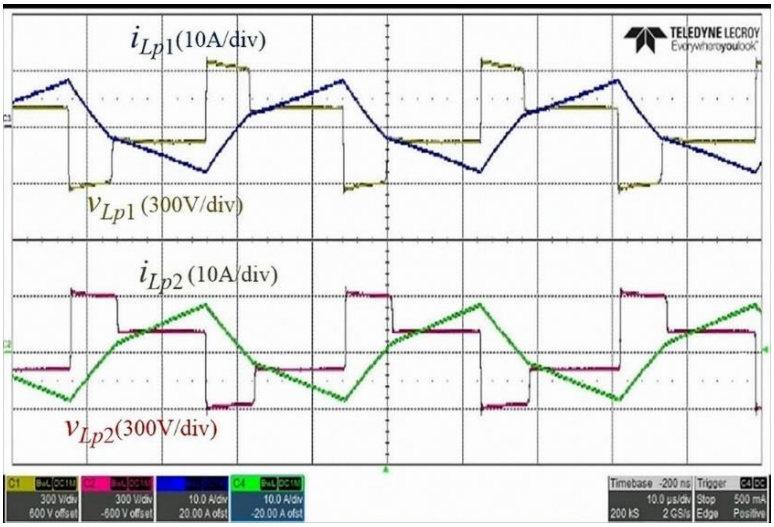

Figure 15. Experimental waveforms of the voltage across the series inductors and the current through the series inductors.

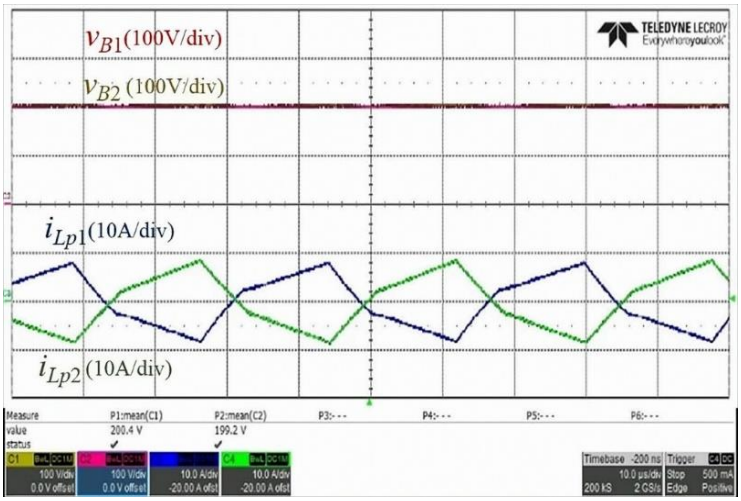

Figure 16. Experimental waveforms of the battery module voltage and current of the transformers.

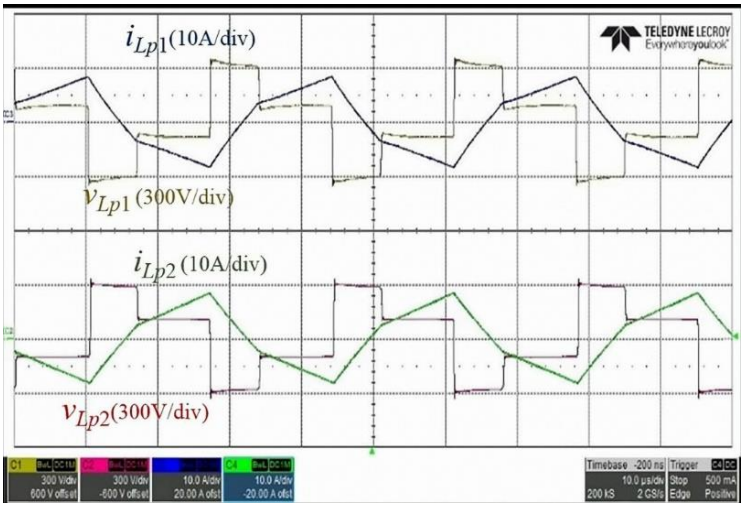

Figure 17. Experimental waveforms of the voltage across the series inductors and the current through the series inductors under unbalanced battery module condition.

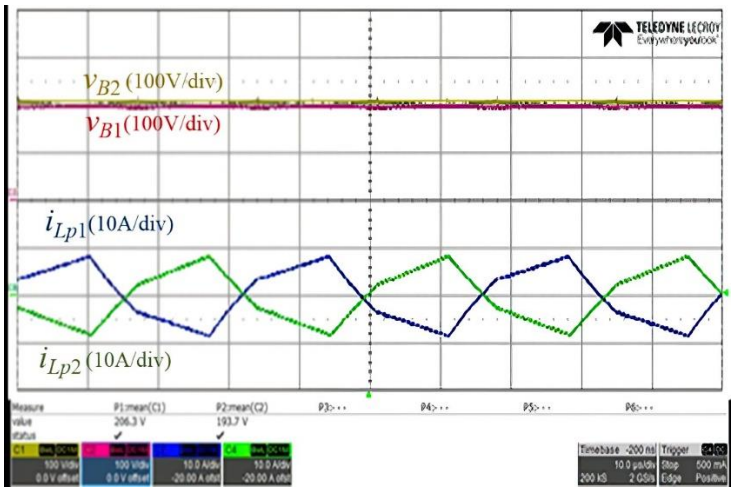

Figure 18. Experimental waveforms of the battery module voltage and current of the transformers under unbalanced battery module conditions.

In order to verify the feasibility of the proposed control strategies, the experimental hardware was also tested for the grid-connected mode and the standalone mode. Waveforms of the H-bridge inverter output voltage v_o, the grid voltage v_{ac}, and the inverter output current i_{ac} are shown in Figure 19. The dotted line indicates the real starting point of entering the standalone mode from the grid-connected mode. Conventionally, it is very common that a current drop or spike can easily occur in this duration when the H-bridge inverter switches the controller from the grid-connected mode to the standalone mode. On the contrary, Figure 19 shows that there is no current drop or spike during the transition. Figure 20 shows the experimental results of the mode transfer between UCM and TPCM for the proposed H-bridge inverter. Waveforms of inverter output voltage v_o, the grid voltage v_{ac}, the inverter output current i_{ac}, and the gate-to-source voltage of S_{r3}, v_{gs_Sr3}, are shown in Figure 20a,b. In Figure 20a, the dotted line indicates the starting point of entering TPCM from UCM. It can be seen that the low-frequency legs return to the lower frequency switching without a current drop or spike, while similar experimental waveforms from TPCM to UCM are shown in Figure 20b.

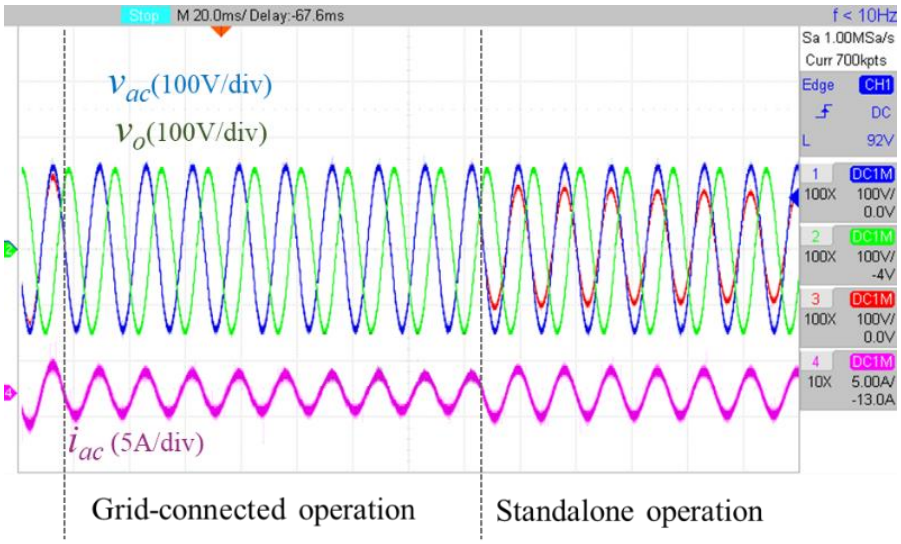

Figure 19. Experimental waveforms of the H-bridge inverter for the grid-connected operation and the standalone operation.

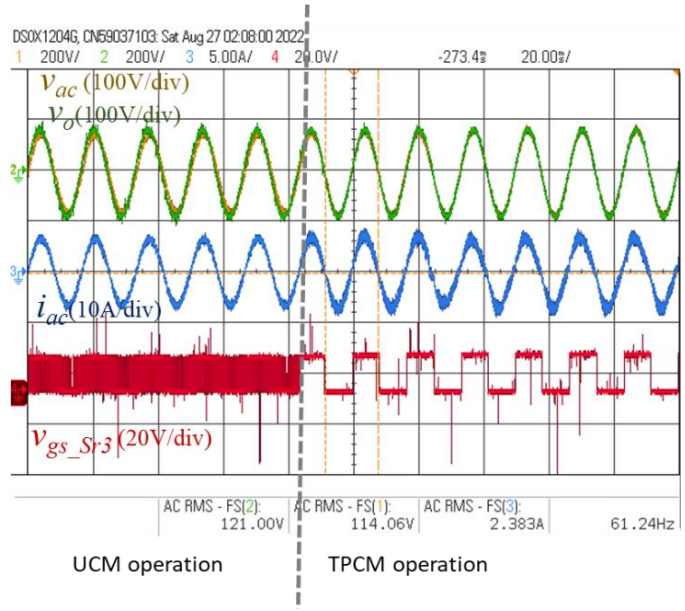

(**a**)

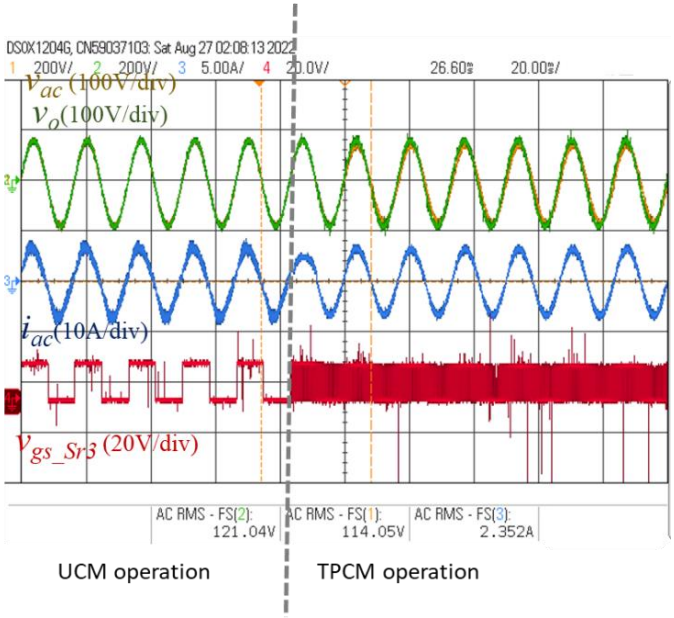

(**b**)

Figure 20. Experimental waveforms of the mode transfer between UCM and TPCM: (**a**) from UCM to TPCM; (**b**) from TPCM to UCM.

Theoretically, by isolating the DC bus voltage of the HBDAB converter, the proposed control strategies can be applied to control the three-phase system. Figure 21 shows the experimental results of the three-phase system for the proposed H-bridge inverter. There are three DC–AC converters connected to a three-phase system. Waveforms of r-phase output voltage v_{ac1}, s-phase output voltage v_{ac2}, r-phase output voltage i_{ac1}, and s-phase output voltage i_{ac2}, are shown in Figure 21. It can be seen that the capability of the unbalanced current control can be achieved for a three-phase system. The power conversion efficiency of the H-bridge inverter under different output power and control modes is shown in Figure 22. The TPCM demonstrated better output performance, with power-conversion efficiency higher than 4% at full load conditions.

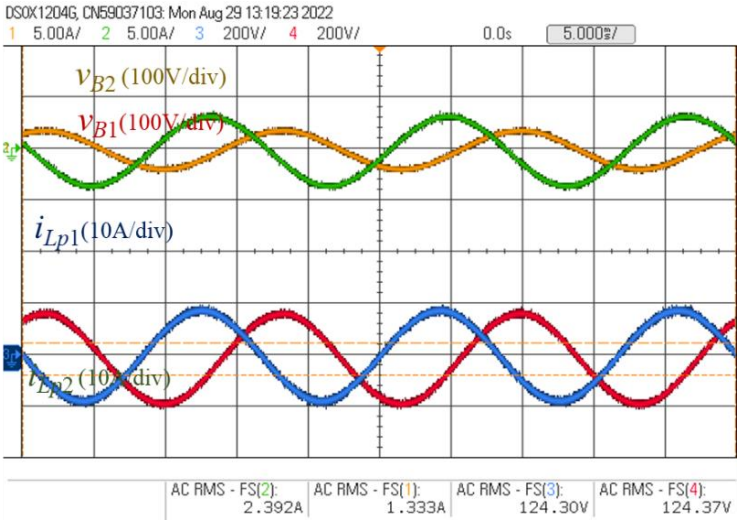

Figure 21. Experimental waveforms of the H-bridge inverter for a three-phase system.

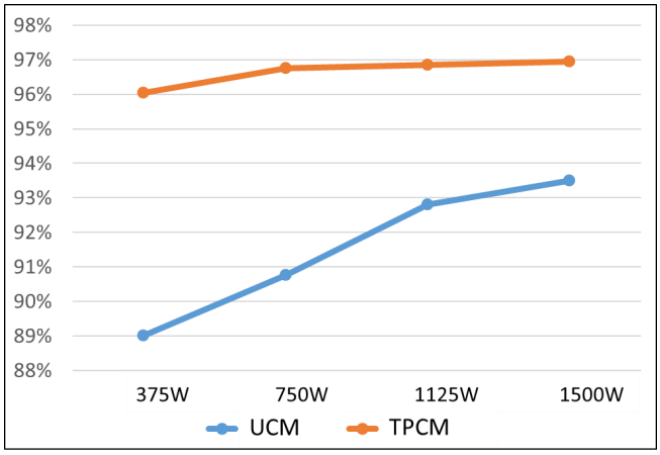

Figure 22. Power conversion efficiency of the H-bridge inverter under different output power and control modes.

4. Conclusions

In this paper, a bidirectional converter with multi-mode control strategies is proposed for a battery energy storage system. The HBDAB converter is designed to achieve the individual power-handling capability required for the battery modules adopted in this paper. The variable-frequency control (VFC) and phase-shift control (PSC) are used to achieve the zero-voltage switching over a wider power range and the battery module balance control capability for BESS. The H-bridge inverter is designed to achieve the DC–AC function with UCM and TPCM control modes. The principle of operation, controller design, and voltage gain analysis are described in this paper. A prototype that is composed of two sets of HBDAB modules and an H-bridge inverter is built and tested to demonstrate the applicability and functionality for BESS. The experimental results obtained from a 1 kW prototype circuit verify the performance of the proposed bidirectional converter.

Author Contributions: Conceptualization, K.-Y.L.; methodology, K.-Y.L., L.-X.C., C.-H.S. and C.-Y.C.; formal analysis, K.-Y.L., K.-H.L., L.-X.C. and C.-H.S.; resources, C.-Y.C.; computer software simulation, L.-X.C. and C.-H.S.; system hardware implementation, K.-H.L., L.-X.C., C.-H.S. and J.-T.L.; writing, K.-Y.L.; review and editing, K.-Y.L. All authors have read and agreed to the published version of the manuscript.

Funding: This research was funded by the Institute of Nuclear Energy Research, Taiwan, grant number NL1110314.

Institutional Review Board Statement: Not applicable.

Informed Consent Statement: Not applicable.

Data Availability Statement: Not applicable.

Conflicts of Interest: The authors declare no conflict of interest.

References

1. Jiang, Q.; Wang, H. Two-time-scale coordination control for a battery energy storage system to mitigate wind power fluctuations. *IEEE Trans. Energy Convers.* **2013**, *28*, 52–61. [CrossRef]
2. Marcos, J.; De la Parra, I.; García, M.; Marroyo, L. Control Strategies to Smooth Short-Term Power Fluctuations in Large Photovoltaic Plants Using Battery Storage Systems. *Energies* **2014**, *7*, 6593–6619. [CrossRef]
3. Li, X.; Hui, D.; Lai, X. Battery energy storage station (BESS)-based smoothing control of photovoltaic (PV) and wind power generation fluctuations. *IEEE Trans. Sustain. Energy* **2013**, *4*, 464–473. [CrossRef]
4. Gao, J.-T.; Shih, C.-H.; Lee, C.-W.; Lo, K.-Y. An Active and Reactive Power Controller for Battery Energy Storage System in Microgrids. *IEEE Access* **2022**, *10*, 10490–10499. [CrossRef]
5. Min, J.; Ordonez, M. Asymmetric parameters design for bidirectional resonant CLLC battery charger. In Proceedings of the 2020 IEEE Energy Conversion Congress and Exposition (ECCE), Detroit, MI, USA, 11–15 October 2020; pp. 5375–5379.
6. Mukherjee, S.; Kumar, A.; Chakraborty, S. Comparison of DAB and LLC DC–DC converters in High-Step-Down Fixed-Conversion-Ratio (DCX) applications. *IEEE Trans. Power Electron.* **2020**, *36*, 4383–4398. [CrossRef]
7. Siebke, K.; Mallwitz, R. Operation mode analysis of the CLLC resonant converter. In Proceedings of the 2019 IEEE 13th International Conference on Compatibility, Power Electronics and Power Engineering (CPE-POWERENG), Sonderborg, Denmark, 23–25 April 2019; pp. 1–6.
8. Liu, J.; Yang, J.; Zhang, J.; Nan, Z.; Zheng, Q. Voltage balance control based on dual active bridge DC/DC converters in a power electronic traction transformer. *IEEE Trans. Power Electron.* **2018**, *33*, 1696–1714. [CrossRef]
9. Higa, H.; Takuma, S.; Orikawa, K.; Itoh, J. Dual active bridge DC-DC converter using both full and half bridge topologies to achieve high efficiency for wide load. In Proceedings of the 2015 IEEE Energy Conversion Congress and Exposition (ECCE), Montreal, QC, Canada, 20–24 September 2015; pp. 6344–6351.
10. Bai, H.; Nie, Z.; Mi, C.C. Experimental comparison of traditional Phase-Shift, Dual-Phase-Shift, and Model-Based control of isolated bidirectional DC–DC converters. *IEEE Trans. Power Electron.* **2010**, *25*, 1444–1449. [CrossRef]
11. Zhao, B.; Song, Q.; Liu, W. Power characterization of isolated bidirectional Dual-Active-Bridge DC–DC converter with Dual-Phase-Shift control. *IEEE Trans. Power Electron.* **2012**, *27*, 4172–4176. [CrossRef]
12. Cho, Y.; Cha, W.; Kwon, J.; Kwon, B. High-Efficiency bidirectional DAB inverter using a novel hybrid modulation for Stand-Alone power generating system with low input voltage. *IEEE Trans. Power Electron.* **2016**, *31*, 4138–4147. [CrossRef]
13. He, P.; Khaligh, A. Comprehensive analyses and comparison of 1 kW isolated DC–DC converters for bidirectional EV charging systems. *IEEE Trans. Transp. Electrif.* **2017**, *3*, 147–156. [CrossRef]
14. Shi, H.; Sun, K.; Wu, H.; Li, Y. A unified State-Space modeling method for a Phase-Shift controlled bidirectional Dual-Active Half-Bridge converter. *IEEE Trans. Power Electron.* **2020**, *35*, 3254–3265. [CrossRef]
15. Wang, Y.; Zhang, Y.; Wang, Y.; Zhu, L.; Guan, Y.; Chen, S.Z.; Zhang, G.; Yang, L. A Dual-Active-Bridge with Half-Bridge submodules DC Solid-State transformer for DC distribution networks. *IEEE J. Emerg. Sel. Top. Power Electron.* **2021**, *9*, 1891–1904. [CrossRef]
16. Wang, Y.; Chen, S.Z.; Wang, Y.; Zhu, L.; Guan, Y.; Zhang, G.; Yang, L.; Zhang, Y. A multiple modular isolated DC/DC converter with bidirectional fault handling and efficient energy conversion for DC distribution network. *IEEE Trans. Power Electron.* **2020**, *35*, 11502–11517. [CrossRef]
17. Shao, S.; Jiang, M.; Ye, W.; Li, Y.; Zhang, J.; Sheng, K. Optimal Phase-Shift control to minimize reactive power for a dual active bridge DC–DC converter. *IEEE Trans. on Power Electron.* **2019**, *34*, 10193–10205. [CrossRef]
18. Pal, A.; Basu, K. A Zero-Current-Switched PWM full bridge DC-DC converter. In Proceedings of the 2019 IEEE Energy Conversion Congress and Exposition (ECCE), Baltimore, MD, USA, 29 September–3 October 2019; pp. 6424–6429.
19. Lin, B.; Du, Y. Analysis, design and implementation of a wide ZVS full-bridge converter. In Proceedings of the TENCON 2015–2015 IEEE Region 10 Conference, Macao, China, 1–4 November 2015; pp. 1–6.
20. Lim, C.; Han, J.; Park, M.; Kim, K.; Moon, G. Phase-Shifted Full-Bridge DC-DC converter with high efficiency and reduced output filter using center-tapped clamp circuit. In Proceedings of the 2019 IEEE Applied Power Electronics Conference and Exposition (APEC), Anaheim, CA, USA, 17–21 March 2019; pp. 1710–1715.
21. Liu, C.; Gu, B.; Lai, J.S.; Wang, M.; Ji, Y.; Cai, G.; Zhao, Z.; Chen, C.L.; Zheng, C.; Sun, P. High-Efficiency hybrid Full-Bridge–Half-Bridge converter with shared ZVS lagging leg and dual outputs in series. *IEEE Trans. Power Electron.* **2013**, *28*, 849–861. [CrossRef]
22. Jeung, Y.; Lee, D. Voltage and current regulations of bidirectional isolated Dual-Active-Bridge DC–DC converters based on a Double-Integral sliding mode control. *IEEE Trans. Power Electron.* **2019**, *34*, 6937–6946. [CrossRef]

23. Huang, J.; Li, Z.; Shi, L.; Wang, Y.; Zhu, J. Optimized modulation and dynamic control of a three-phase dual active bridge converter with variable duty cycles. *IEEE Trans. Power Electron.* **2019**, *34*, 2856–2873. [CrossRef]
24. Shah, S.S.; Iyer, V.M.; Bhattacharya, S. Exact solution of ZVS boundaries and AC-Port currents in dual active bridge type DC–DC converters. *IEEE Trans. Power Electron.* **2019**, *34*, 5043–5047. [CrossRef]
25. Chaudhury, T.; Kastha, D. A high gain multiport DC–DC converter for integrating energy storage devices to DC microgrid. *IEEE Trans. Power Electron.* **2020**, *35*, 10501–10514. [CrossRef]
26. Wang, L.; Lam, C.S.; Wong, M.C. Analysis, control, and design of a hybrid grid-connected inverter for renewable energy generation with power quality conditioning. *IEEE Trans. Power Electron.* **2018**, *33*, 6755–6768. [CrossRef]
27. Brandao, D.I.; Araujo, L.S.; Alonso, A.M.; Dos Reis, G.L.; Liberado, E.V.; Marafão, F.P. Coordinated control of distributed three- and single-phase inverters connected to three-phase three-wire microgrids. *IEEE J. Emerg. Sel. Top. Power Electron.* **2020**, *8*, 3861–3877. [CrossRef]
28. Nejabatkhah, F.; Li, Y.W. Flexible unbalanced compensation of three-phase distribution dystem using single-phase distributed generation inverters. *IEEE Trans. Smart Grid* **2019**, *10*, 1845–1857. [CrossRef]
29. Budiwicaksana, L.A.; Ardriani, T.; Furqani, J.; Rizqiawan, A.; Dahono, P.A. Improving inverter output current controller under unbalanced conditions by using virtual impedance. *IEEE Access* **2021**, *9*, 162359–162369. [CrossRef]
30. Chen, L.X.; Lin, J.T.; Lo, K.Y. An interleaved DAB converter for battery energy storage system. In Proceedings of the 2021 IEEE International Future Energy Electronics Conference (IFEEC), Taipei, Taiwan, 16–19 November 2021; pp. 1–5.
31. Mi, C.; Bai, H.; Wang, C.; Gargies, S. Operation, design and control of dual H-bridge-based isolated bidirectional DC-DC converter. *IET Power Electron.* **2008**, *1*, 507–517. [CrossRef]
32. Qi, N.; Yin, Y.; Dai, K.; Wu, C.; Wang, X.; You, Z. Comprehensive optimized hybrid energy storage system for long-life solar-powered wireless sensor network nodes. *Appl. Energy* **2021**, *290*, 116780. [CrossRef]